Canalization of circuit assembly by δ-protocadherins in the zebrafish optic tectum

Sayantanee Biswas[1], Michelle R. Emond[1], Grace S. Philip and James D. Jontes[1,*]

[1]Department of Biological Chemistry and Pharmacology
Ohio State University Wexner College of Medicine
Columbus, OH 43210

*corresponding author: jontes.1@osu.edu

Abstract

Neurons are precisely and reproducibly assembled into complex networks during development. How genes collaborate to guide this assembly remains an enduring mystery. In humans, large numbers of genes have been implicated in neurodevelopmental disorders that are characterized by variable and overlapping phenotypes. The complexity of the brain, the large number of genes involved and the heterogeneity of the disorders makes understanding the relationships between genes, development and neural function challenging. Waddington suggested the concept of canalization to describe the role of genes in shaping developmental trajectories that lead to precise outcomes[1] . Here, we show that members of the δ-protocadherin family of homophilic adhesion molecules, Protocadherin-19 and Protocadherin-17, contribute to developmental canalization of visual circuit assembly in the zebrafish. We provided oriented visual stimuli to zebrafish larvae and performed *in vivo* 2-photon calcium imaging in the optic tectum. The latent dynamics resulting from the population activity described a circular manifold. Among different wild type larvae, these dynamics were remarkably similar, allowing quantitative comparisons within and among genotypes. In both Protocadherin-19 and Protocadherin-17 mutants, the latent dynamics diverged from wild type. Importantly, these deviations could be averaged away, suggesting that the loss of these adhesion molecules leads to stochastic phenotypic variability and introduced disruptions of circuit organization that varied among individual mutants. These results provide a specific, quantitative example of canalization in the development of a vertebrate neural circuit, and suggest a framework for understanding the observed variability in complex brain disorders.

33 ***Introduction***

34 Despite their immense complexity, vertebrate brains are highly organized and exhibit a
35 conserved, stereotyped architecture. Distinct brain regions comprise canonical circuits that carry out
36 well-defined functions, which are conserved both within and between species[2,3] . The assembly of these
37 conserved circuits is robust to genetic and environmental variation, as well as natural biological
38 heterogeneity. This allows the brains of distinct individuals to perform the same tasks, even though they
39 are not identical at the level of neurons and synapses, or in their particular developmental histories. The
40 mechanisms that confer robust circuit development in the face of these multiple sources of variability are
41 poorly understood[4,5] .

42 In the case of neurodevelopmental disorders, such as schizophrenia and autism, the relationship
43 between conserved structure and conserved function breaks down. Characterized by profound
44 disturbances in normal brain function, some evidence suggests that these disorders are
45 "connectopathies," arising from disruption of the underlying network topology[6–10] . While a large number
46 of genes have been linked to developmental brain disorders, understanding the relationship of genotype
47 to phenotype is challenging. In addition to natural biological variability, these disorders are plagued by
48 variability in penetrance and expressivity[11,12] . Moreover, putatively distinct disorders have amorphous
49 boundaries, overlapping with one another and exhibiting comorbidities[13], as well as sharing genetic
50 origins[14–16] . Collectively, these sources of variation mask the relationships between gene function,
51 circuit organization and neural activity. These same issues make interpretation of studies in animal
52 models similarly challenging.

53 Protocadherin-19 is a member of the δ-protocadherin family of homophilic cell adhesion
54 molecules[17–19] . In humans, mutations in *PCDH19* are linked to schizophrenia and autism[20,21] , and cause
55 a developmental epileptic encephalopathy[22,23]. To investigate how mutations in *pcdh19* or the related
56 *pcdh17* affect neural development, we used visual stimulation and *in vivo* 2-photon calcium imaging in
57 the optic tectum of the larval zebrafish. We show that the neuronal population responses to oriented
58 sinusoidal gratings define neural dynamics that are strongly stereotyped among wild type larvae. In
59 mutants, these dynamics are altered, reflecting stochastic deviations in circuit organization. Our results

are consistent with a role for protocadherins in canalization of development, contributing to robustness of circuit assembly. This can provide a conceptual framework for understanding the variability associated with neurodevelopmental disorders.

Results

Moving stimuli, such as moving lines, spots or gratings, elicit robust responses in the optic tectum of zebrafish[24–27]. To record the activity of tectal neurons, we generated a transgenic line that *pan*-neuronally expresses a nuclear localized jGCaMP8s (Histone H2B-GCaMP8s). These transgenic larvae were mounted in a custom imaging chamber **(Fig. 1a**), and we elicited visual responses by projecting a sequence of drifting sinusoidal gratings (12 directions rotated at 30º intervals) onto an adjacent translucent screen (**Fig. 1b,c**). Two-photon image stacks spanning the optic tectum (7 optical sections at 10 µm spacing) were collected at 1 Hz (**Fig. 1d**), allowing us to sample population activity. We used constrained non-negative matrix factorization (CNMF) with CaImAn[28] to automatically segment images and extract fluorescence traces from visually-responsive neurons (**Fig. 1e,f**). For further analysis, the neural responses were averaged across three trials (**Fig. 1g**). Overall, we obtained 2506 visually responsive neurons (278.4±26.6, n=9).

It is now widely understood that sensory processing and motor control are encoded by neuronal population dynamics, rather than the activities of individual neurons[29,30] . These latent dynamics consist of a small number of covariation patterns, or neural modes, which describe a neural manifold within a low-dimensional subspace[31–33] . To explore the structure of tectal population dynamics in response to visual stimulation, we performed linear dimensionality reduction with principal component analysis (PCA) (**Fig. 2a**). For n neurons, PCA reduces the data from an n-dimensional space to a more compact k-dimensional space. We found that the first five neural modes captured 89.9±1.8% (n=9; mean ± std.dev.) of the variance in our wild type data (**Fig. 2b**), and our subsequent analyses are confined to these five neural modes. Each axis represents a significant pattern of neuronal covariation that is activated to varying extent during the presentation of visual stimuli, and projection of the original neural data onto these axes describes the latent dynamics evoked by visual stimulation (**Fig. 2c**). To determine how

consistent the neural responses are in individual larvae, the latent dynamics were obtained for individual trials, and the Pearson's correlation (r) between individual trials was calculated along each dimension (**Fig. 2c,d**). The mean trial-to-trial correlation was greater than 0.9 across all 5 neural modes (**Fig. 2d**). Recent evidence suggests that the similarity of neural architecture among individuals gives rise to similar latent dynamics for a given stimulus or motor task[34] . In mammals, latent dynamics are estimated from a small subsample of neurons, which varies from individual to individual. In such cases, the latent dynamics from different animals need to be aligned using a procedure such as canonical correlation analysis[34,35] . Here, we image a relatively large proportion of visually-responsive neurons and sample among the same neuronal types across different fish, obviating the need for alignment. For each wild type individual, we determined the latent dynamics from trial averaged responses (**Fig. 2e**). To quantify the similarity of the dynamics among the pool of wild types, we generated the averaged response, then calculated Pearson's correlation between this average and the dynamics of each individual (**Fig. 2e,f**). The mean correlation along each neural mode was nearly as high as for trial-to-trial correlations (**Fig. 2c,d**), indicating that the similarity of dynamics among individuals is comparable to the similarity of successive trials in the same individual. Thus, the latent dynamics elicited by visual stimulation is stereotyped across different zebrafish larvae, facilitating comparisons within and among experimental groups. When plotted in three dimensions, the latent dynamics from individual larvae describe a rosette shaped trajectory, with each leaf representing the response to a direction of grating drift (**Fig. 2g,h**). The averaged dynamics yielded a smooth, roughly circular, trajectory in three dimensions (**Fig. 2i**). Thus, the population response to our simple stimulus presentation, encodes the direction of motion on a neural manifold that is preserved across zebrafish larvae.

To investigate the involvement of *pcdh19* in the assembly of visual circuitry we used two, distinct *pcdh19* mutant alleles. We previously introduced an indel lesion near the 5' end of exon1 shortly after the sequence encoding the signal peptide[36,37] , resulting in a complete lack of functional Pcdh19 ($pcdh19^{-10bp}$). In addition, we have generated a new "promoterless" *pcdh19* allele, which lacks ~4kb of genomic sequence, spanning the basal promoter, 5'UTR and the ATG start codon in exon 1 ($pcdh19^{\Delta prom}$). While both alleles completely eliminate the production of Pcdh19 protein, evidence suggests that indel

114 mutations, like *pcdh19*$^{-10bp}$, can elicit compensatory mechanisms arising from nonsense-mediated RNA
115 decay[38,39] . Both of these mutant lines were crossed into our *Tg(elav3l:H2B-GCaMP8s)* line. As above,
116 we performed calcium imaging on homozygous mutants during visual stimulation, and computed the
117 latent dynamics for each mutant from the trial averages of visually responsive neurons (**Fig. 3a,b**). To
118 determine whether the mutant groups differed from wild type in their visual responses, we correlated the
119 trial-averaged dynamics from each individual mutant with the wild type group average along each neural
120 mode (**Fig. 3c**). Both *pcdh19*$^{-10bp}$ and *pcdh19*$^{\Delta prom}$ showed decreased correlation with the group average
121 (**Fig. 3c**), although this varied by neural mode between the two mutants. The *pcdh19*$^{-10bp}$ larvae showed
122 the greatest change along the second neural mode, while *pcdh19*$^{\Delta prom}$ mutants exhibited significant
123 differences along neural modes 2-5 (**Fig. 3c**). The response to drifting sinusoidal gratings diverged from
124 wild type for both *pcdh19* mutants, as the trajectories of individual mutant fish were less correlated to the
125 wild type average than were individual wild type fish. To determine whether individual mutants described
126 similar or distinct trajectories, we calculated pairwise correlations between larvae within an experimental
127 group. If mutants converged on a distinct, but stereotyped, circuit organization, then their intra-group
128 correlation should be similar to the intra-group correlations of the wild type group. Alternatively, if the
129 divergence of the mutants from wild type is due to stochastic variations, then the intra-group correlations
130 should be lower and exhibit an increased variance. Consistent with stochastic variation, the *pcdh19*
131 mutants exhibit lower intra-group correlations than wild type larvae (**Fig. 3d**). When visualized in three
132 dimensions, the trajectories from individual *pcdh19*$^{\Delta prom}$ mutants differ dramatically from the stereotyped
133 paths of wild type larvae (**Fig. 2g,h**), and diverge from each other (**Fig. 3e,f**). However, despite the
134 variability of the individual mutants, averaging within a genotype suppresses this variation and gives rise
135 to averaged dynamics that are strongly correlated with wild type (**Fig. 3g**). This suggests that the effect
136 of *pcdh19* loss on visual processing is best understood as stochastic developmental noise, as this noise
137 can be suppressed by averaging (**Fig. 3g**).

138 Pcdh19 is a member of a small family of related δ2-pcdhs. To determine if mutations in other δ2-
139 pcdhs also affect visual responses in the optic tectum, we recorded the response to visual stimulation in
140 mutants lacking *pcdh17* (*pcdh17*$^{-5bp}$)[37] . As above, we used the trial averaged neuronal responses to

141 compute the latent dynamics along the first five neural modes (**Fig. 4a**). Similar to the *pcdh19* mutants,
142 the latent dynamics exhibited by *pcdh17*$^{-5bp}$ mutants was less correlated with the wild type average (**Fig.**
143 **4a**), although the differences were not statistically significant (**Fig. 4b**). To measure the intra-group
144 variation exhibited by the *pcdh17*$^{-5bp}$ mutants, we determined pairwise correlations along each neural
145 mode (**Fig. 4c**). Although there was a uniform decrease in pairwise correlation among the *pcdh17*$^{-5bp}$
146 mutants, this was only significant for neural mode 5 (**Fig. 4c**). This observed intra-group noise was
147 eliminated by averaging, as the *pcdh17*$^{-5bp}$ group average exhibited high correlation with the wild type
148 average (**Fig 4d**). As each mutant genotype showed a reduced intra-group correlation, it is possible that
149 this increased variation is due to unreliable or noisy neuronal responses. To determine whether the
150 tectal responses to visual stimulation are reliable, we determined the between-trial correlations for each
151 neural mode within each experimental group (**Fig. 4e**). We found no significant difference in the
152 between-trial consistency of the population dynamics in the mutant groups, compared to wild type (**Fig.**
153 **4e**). This suggests that each mutant network is responding reliably and reproducibly to repeated
154 presentations of a given stimulus, yet deviates randomly from the wild type. To quantify the within-group
155 variance, we generated histograms of all pairwise correlation coefficients within each experimental group
156 (**Fig. 4f**). While the distribution of correlation coefficients for the wild type group is narrow and
157 concentrated at higher correlations, the mutants all exhibit significantly broader distributions (**Fig. 4f**). To
158 provide a metric for the overall similarity of latent dynamics among different larvae, we calculated the
159 mean r of individual correlations across the five neural modes for each genotype (**Fig. 4g**). If the
160 computed dynamics are empirical estimates of the neural manifold, then this summary r should measure
161 the similarity of an individual manifold to the averaged wild type manifold. In the case of each mutant
162 genotype, the dynamics are significantly different from wild type, although the effect is more robust for
163 the *pcdh19*$^{\Delta prom}$ mutants (**Fig. 4g**). While the variations along individual neural modes are not considered
164 to be statistically significant for the *pcdh17*$^{-5bp}$ mutants, the aggregate impact on the shape of the neural
165 manifold is significant (**Fig. 4g**). Thus, loss of either *pcdh19* or *pcdh17* alters the neural population
166 response to visual stimulation, by introducing stochastic perturbations into circuit assembly. Our data are
167 consistent with the idea that δ2-pcdhs contribute to canalization of the developing optic tectum (**Fig. 4h**).

168 The absence of these molecules allows configurations of the network that would otherwise be
169 inaccessible or improbable.
170
171 ***Discussion***
172 The δ2-pcdhs comprise a subfamily of homophilic cell adhesion molecules within the cadherin
173 superfamily that are associated with neurodevelopmental disorders in humans[40,41] . Among the five δ2-
174 pcdhs in mammals, all are linked to human disorders: *PCDH8* and *PCDH10* are linked to autism[42,43] , a
175 genomic deletion encompassing *PCDH18* caused severe intellectual disability[44] , *PCDH17* is implicated
176 in mood disorders[45] , and mutations in *PCDH19* cause a developmental epileptic encephalopathy[22,23] ,
177 and are associated with autism and schizophrenia [20,21] . We previously used large-scale *in vivo* calcium
178 imaging of spontaneous activity and network analysis to show that zebrafish mutants lacking *pcdh19* had
179 defects in network topology[46] . Subsequently, others showed that mutant rodents and zebrafish larvae
180 were hyperexcitable[47,48] , and that mutant rodents showed increased network synchrony[47] . Here, our
181 results show that loss of either *pcdh19* or *pcdh17* impairs visual processing in the optic tectum of the
182 larval zebrafish.
183 Our data show that the response of the larval optic tectum to moving sinusoidal gratings is
184 encoded by low-dimensional dynamics that are confined to a neural manifold. These dynamics are highly
185 stereotyped among wild type individuals. It was recently shown that dynamics are preserved across
186 individuals within a species, but these dynamics need to be aligned using a procedure such as canonical
187 correlation analysis[34], due to the fact that the latent dynamics are estimated from only a small subsample
188 of neurons that vary among animals. Here, we image a substantial proportion of the visually responsive
189 neurons in the optic tectum. Consequently, the latent dynamics derived from different individuals do not
190 require further alignment. This allows the complex neural responses of hundreds of neurons in different
191 animals to be reduced to a common set of activity patterns that can be quantitatively compared within
192 and between genotypes. The variation among wild type individual larvae is very low, indicating that
193 development within a population gives rise to an ensemble of equivalent networks that differ in the

194 precise number, morphology and connectivity of the constituent neurons, but whose overall functional
195 variation is small.

196 Elimination of either *pcdh19* or *pcdh17* leads to altered latent dynamics. The stereotyped neural
197 response that characterizes the population of wild type larvae is degraded in the mutants, whose
198 dynamics are less well correlated to the averaged wild type response. The latent dynamics among the
199 mutant genotypes varies by individual. As a consequence, within a mutant group, individuals are much
200 less similar to each other than the pool of wild type larvae are to each other. Additionally, this stochastic
201 variability is masked in a group average, as the deviations specific to an individual can be averaged
202 away. This implies that the loss of Pcdh19 or Pcdh17 does not lead to a particular, alternative network
203 structure, but to a stochastic array of alternatives. Thus, the effects of the *pcdh19* and *pcdh17* mutations
204 are best understood as an increase in developmental noise, leading to an increase in phenotypic
205 variability. Our data show that the effects of a well-defined genetic lesion on a simple, highly stereotyped
206 network can be stochastic. While both $pcdh19^{-10bp}$ and $pcdh19^{\Delta prom}$ mutants result in a complete loss of
207 Pcdh19 protein, their effects on the optic tectum are not identical. The phenotype associated with
208 Pcdh19 loss in the $pcdh19^{\Delta prom}$ line is significantly more severe than in the $pcdh19^{-10bp}$ line. Combined
209 with the observation that the magnitude of the impact of indel mutations in $pcdh19^{-10bp}$ and $pcdh17^{-5bp}$ is
210 similar, this suggests that the difference could be due to the activation of compensatory mechanisms by
211 the indel mutations that are absent in the promoterless allele. This may indicate a further source of
212 variability in understanding neural disorders and in the study of relevant genes in animal models, as even
213 alternative "null" mutations may give rise to distinct phenotypes.

214 In evolution, strong selective pressures prevent the accumulation of mutations that have an
215 adverse impact on phenotypic fitness. Release of a selective pressure can then lead to an increase in
216 allelic and phenotypic diversity within a population. By analogy, our results suggest that Pcdh19 and
217 Pcdh17 suppress variation in the development of tectal circuitry. Loss of either protocadherin releases a
218 constraint on circuit assembly, allowing stochastic variation in circuit organization and function. These
219 results suggest that Pcdh19 and Pcdh17 contribute to developmental robustness by canalizing circuit
220 assembly and limiting developmental variability. While canalization is most commonly discussed in terms

221 of gene regulatory networks buffering against adverse genetic or environmental effects[49,50] , we suggest
222 that the protocadherins may buffer against the formation of inappropriate connections and help guide
223 circuit assembly toward an optimal outcome. These results suggest that while the heterogeneity
224 observed in neurodevelopmental disorders is often attributed to polygenic effects, it could also be due to
225 decanalization of circuit assembly and stochastic degradation of circuit function.
226

227 ***Methods***

228 *Zebrafish maintenance and generation of lines*

229 Adult zebrafish (Danio rerio) were maintained at ~28.5°C and staged according to Westerfield
230 (1995). All animal procedures were performed in accordance with the Ohio State University animal care
231 committee's regulations. We previously generated lines harboring germline mutations of *pcdh19*
232 (*pcdh19*^{os51})[36] and *pcdh17* (*pcdh17*^{os69})[37] .

233 The *pcdh19*$^{\Delta prom}$ mutant line (*pcdh19*^{os77}) was established by co-injecting ribonucleoprotein
234 complexes (Integrated DNA Technologies) consisting of Cas9 protein and gRNAs targeting a site in the
235 5' end of *pcdh19* exon1 (GGGCTCAGATTAACCCATCG) and ~4 kb upstream of the ATG start codon
236 (CTGTTGTGAGCTAGTTACCA), which is predicted to eliminate the promoter region. Founders were
237 identified by PCR and sequenced, confirming the large genomic deletion. Like the *pcdh19*$^{-10bp}$ line,
238 Western blots confirmed that the homozygous *pcdh19*$^{\Delta prom}$ line produced no Pcdh19 protein.

239 The plasmid *Tol2-elavl3:H2B-GCaMP8s* was assembled using the following plasmids: Tol2-
240 elavl3-GCaMP6s (a gift from Misha Ahrens; Addgene plasmid # 59530 ; http://n2t.net/addgene:59530 ;
241 RRID:Addgene_59530), CMV:Histone H2B-mGL (H2B-mGreenLantern was a gift from Gregory Petsko;
242 Addgene plasmid # 164464 ; http://n2t.net/addgene:164464 ; RRID:Addgene_164464), and
243 CMV:jGCaMP8s (gift from GENIE Project; Addgene plasmid # 162371 ; http://n2t.net/addgene:162371 ;
244 RRID:Addgene_162371). Along with mRNA encoding Tol2 transpose, this plasmid was co-injected into
245 1 cell stage *nacre* embryos in order to establish the transgenic line *Tg(elavl3:H2B-GCaMP)*^{os78}. This
246 transgenic line was crossed with the *pcdh19*$^{-10bp}$, *pcdh19*$^{\Delta prom}$and *pcdh17*$^{-5bp}$ mutant lines.

247

248 *Calcium imaging*

249 Unanaesthetized 6 days-post-fertilization (dpf) larvae were embedded dorsal side up in 2% low
250 melting point agarose. Imaging was performed on a custom-built resonant-scanning 2-photon
251 microscope. Briefly, 920nm excitation was provided by an Axon920-TPC laser (Coherent, Inc.). We
252 used a Nikon Apochromat 25x/1.1NA water-immersion objective for imaging. The resonant scan-head
253 and controller, 3DMS robotic stage, Hamamatsu GaAsP photomultiplier tubes and power supply were
254 obtained from Sutter Instruments (www.sutter.com). A piezo-electric objective positioner (nPFocus250)
255 was obtained from nPoint (www.npoint.com). The microscope was run with ScanImage 5.2[51] (Vidrio
256 Technologies). All other parts were obtained from Thorlabs (www.thorlabs.com). Image stacks of 7
257 optical sections (512x512), spaced at 10 μm, were collected at 1 s intervals, with a pixel size of 0.65 μm.
258 For each group, we included data from 9-13 larvae, which is in line with the number of fish used in
259 comparable studies[52–54] . These were derived from at least two, separate crosses.

260

261 *Visual stimulation*

262 Visual stimuli were programmed in Python, using PsychoPy3 (https://psychopy.org). Moving sinusoidal
263 gratings were presented for 5 seconds, with 10 seconds of a neutral gray background in between each
264 direction, which were rotated at 30° intervals. The stimulus set was presented three times, with 50
265 seconds in between each presentation. Stimuli were projected onto a translucent screen 2.5 cm from the
266 larvae using a Rif6 cube picoprojector (rif6.com). The stimulus occupied ~104° of the visual field.

267

268 *Data analysis*

269 We used CaImAn-MATLAB for processing of calcium imaging movies[28] , including non-rigid
270 motion correction with NoRMCorre[55] . First, sequences of image stacks (735 stacks of 7 planes) were
271 re-formatted to movies of image planes (7 stacks of 735 timepoints). These were motion corrected and
272 inspected for motion artifacts. Movies that exhibited z-drift or other defects were discarded. Brightness
273 and contrast were adjusted and then images were masked in order to analyze only the left (visually-

responsive) hemi-tectum. CaImAn was used to segment movies and extract ΔF/F fluorescence traces. Cells that were responsive to the visual stimuli in each of the three trials were selected for further analysis.

Principal Component Analysis was performed on individual datasets. As ~90% of the variance was explained by the top 5 principal components (neural modes), we restricted our analysis to these. We projected the original neural responses onto these new basis vectors. The order of neural modes varied among datasets, as did the sign of the neural mode. We established a standard order and inspected each dataset to ensure a common order and sign for the neural modes. For comparisons of neural modes among datasets, we used Pearson's correlation, r[34,35] . First, we averaged dynamics along each neural mode to generate a wild type average. Correlation of neural modes from individual larvae to the averaged neural modes provided a measure of the variance. As an alternative measure of the variance in the datasets, each individual set of neural modes was correlated to all others within a group. This pairwise correlation describes how much latent dynamics varied among individuals within a genotype. To generate a single measure of similarity of latent dynamics between an individual and the wild type average, we averaged the correlation coefficients across the 5 neural modes. For comparisons, statistical significance was determined using Dunnett's test. For the comparison of distributions of r, we used a Dunn's test. All statistical analysis was performed in JMP Pro 17.

Acknowledgements

This work was supported by grant R21EY034706 from the National Eye Institute and R01GM141280 from the National Institute of General Medical Sciences to JDJ. We would like to thank Marcus Nichols for support with zebrafish maintenance and husbandry.

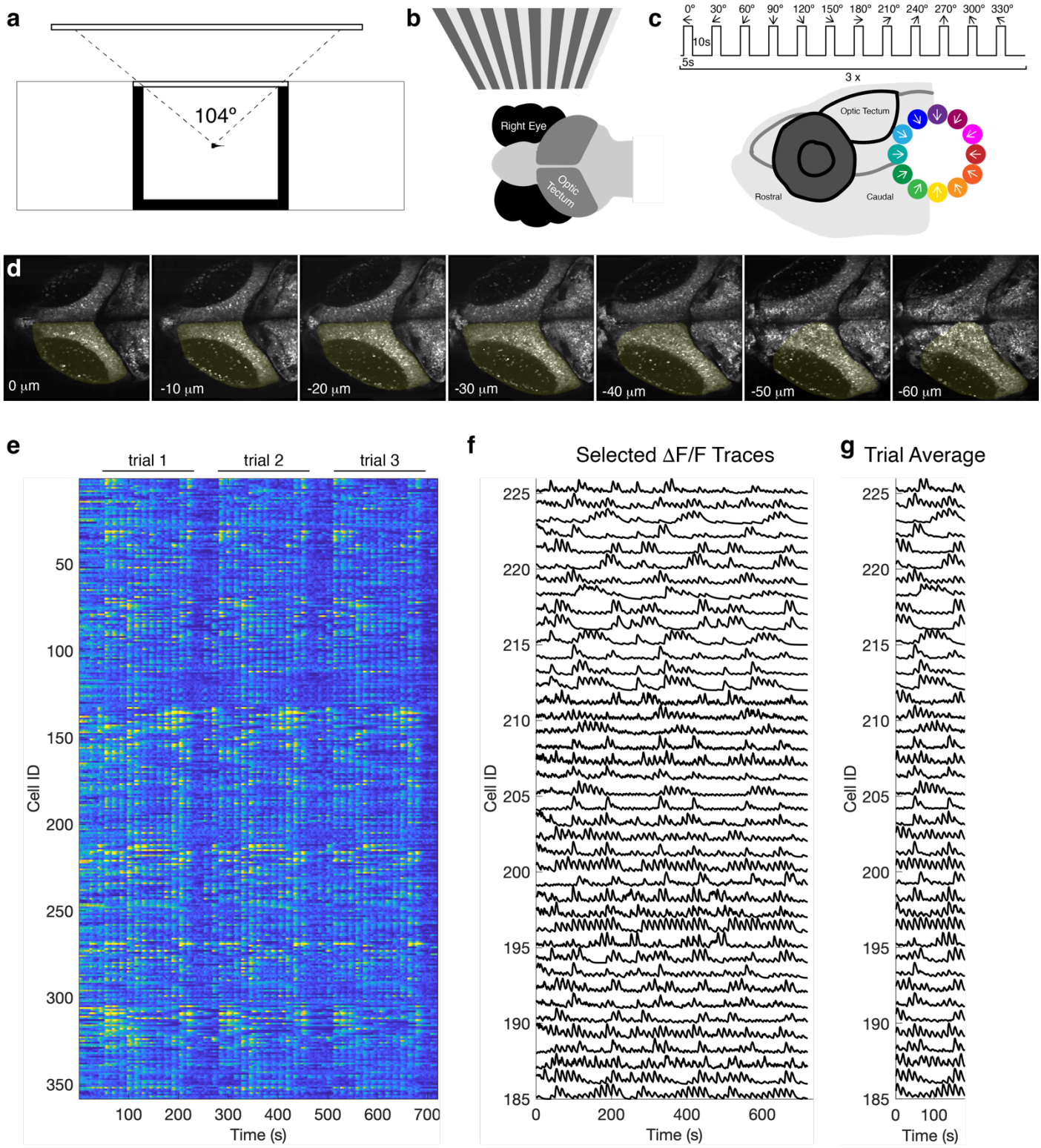
a
104°
b
Right Eye
Optic Tectum
c
0° 30° 60° 90° 120° 150° 180° 210° 240° 270° 300° 330°
10s
5s
3 x
Optic Tectum
Rostral
Caudal
d
0 μm
-10 μm
-20 μm
-30 μm
-40 μm
-50 μm
-60 μm
e
trial 1
trial 2
trial 3
Cell ID
Time (s)
f
Selected ΔF/F Traces
Cell ID
Time (s)
g
Trial Average
Cell ID
Time (s)

Figure 1. Calcium-imaging of neural responses to oriented sinusoidal gratings.

a. *Schematic of the experimental setup. A 6dpf larva is embedded in agarose in an imaging chamber, allowing 104º view of a projection screen.*

b. *The visual stimuli are presented to the right eye and the neural responses are visualized in the contralateral (left) hemi-tectum.*

c. *The stimulation protocol is a series of 5s on 10s off of a moving sinusoidal grating, 12 directions spaced at 30º intervals to encompass the full 360º. This is repeated three times. Below is a lateral view of the head of a zebrafish larva. The inset shows the directions of motion of sinusoidal gratings with reference to the rostro-caudal axis of the fish. The direction color-code is used throughout the paper.*

d. *Image stacks consisting of 7 optical sections spaced at 10 µm were collected at 1s intervals. Shown are average intensity images of individual planes from a timelapse sequence collected in a 6 dpf transgenic larva, Tg(elav3l:HistoneH2B-GCaMP8s). The visually-responsive hemi-tectum is outlined in yellow.*

e. *Example data showing all the fluorescence traces from visually-responsive neurons collected from one larva.*

f. *$\Delta F/F$ traces selected from those shown in* ***e****.*

g. *Responses were averaged across the three trials. Shown are the trial averages from the traces in* ***f****.*

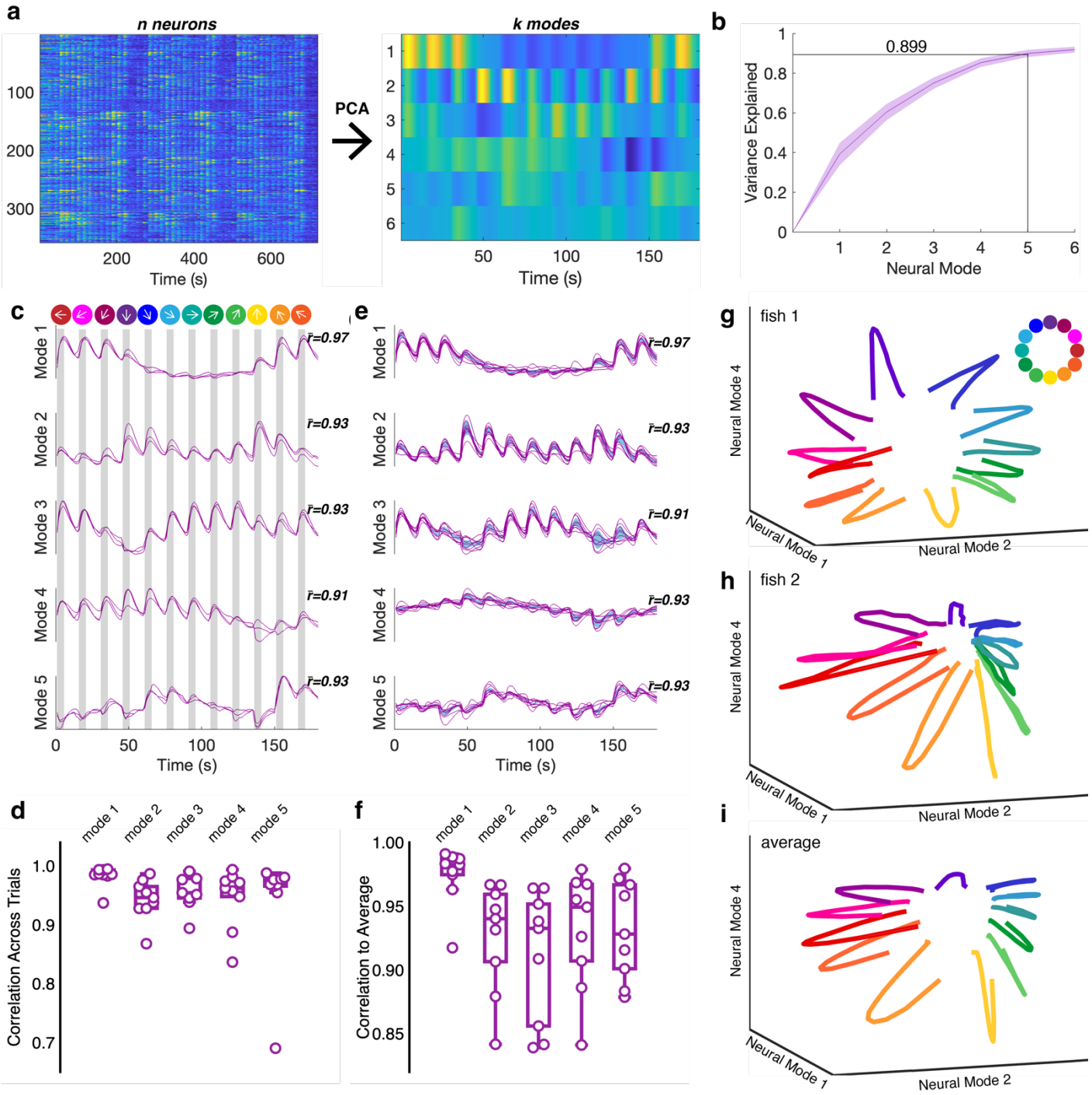
a
n neurons
k modes
PCA
Time (s)
b
0.899
Variance Explained
Neural Mode
c
Mode 1
Mode 2
Mode 3
Mode 4
Mode 5
r̄=0.97
r̄=0.93
r̄=0.93
r̄=0.91
r̄=0.93
Time (s)
e
r̄=0.97
r̄=0.93
r̄=0.91
r̄=0.93
r̄=0.93
Time (s)
g
fish 1
Neural Mode 4
Neural Mode 1
Neural Mode 2
h
fish 2
Neural Mode 4
Neural Mode 1
Neural Mode 2
d
mode 1
mode 2
mode 3
mode 4
mode 5
Correlation Across Trials
f
mode 1
mode 2
mode 3
mode 4
mode 5
Correlation to Average
i
average
Neural Mode 4
Neural Mode 1
Neural Mode 2

Figure 2. Latent dynamics in the optic tecta of zebrafish larvae in response to visual stimulation.
a. *Illustration of our approach to data analysis. Datasets such as the one shown on the left consisted of fluorescence traces from n neurons. These were trial averaged and the dimensionality of the trial averaged data was reduced using PCA. The new k dimensions are referred to as neural modes.*
b. *The first 5 neural modes explain ~90% of the variance in the data. The shaded area represents the standard deviation, n=9).*
c. *Shown are the latent dynamics of an individual wild type larva for the first 5 neural modes. The latent dynamics were calculated independently for each of the three trials. The mean correlation of the dynamics among the individual trials to the trial average is shown as $\bar{r}$. The presentation of each stimulus is shown as a gray bar, and the direction of each stimulus is shown at the top.*
d. *Graph summarizing the mean correlations across trials along each mode for the wild type larvae (0.98±0.006, mode 1; 0.94±0.012, mode 2; 0.96±0.01, mode 3; 0.95±0.017, mode 4; 0.94±0.032, mode 5 ;n=9)*
e. *Latent dynamics determined from trial averaged data. Traces (purple) are the dynamics from individual larvae and the shaded area (blue) is the variance for the wild type group. The value, $\bar{r}$, represents the mean correlation of each individual neural mode to the mean dynamics averaged across the group (see **f**).*
f. *Summary of the correlation between individual larvae and the group average along neural modes (0.97±0.008, mode 1; 0.93±0.014, mode 2; 0.91±0.017, mode 3; 0.93±0.015, mode 4; 0.93±0.013, mode 5; n=9).*
g,h. *Three-dimensional representation of latent dynamics for two, individual larvae. Each color represents a direction of motion for the visual stimulus. The excursions of neural trajectories during stimulus presentation describes a roughly circular neural manifold.*
i. *A three-dimensional representation of latent dynamics averaged across the wild type group (n=9).*

412

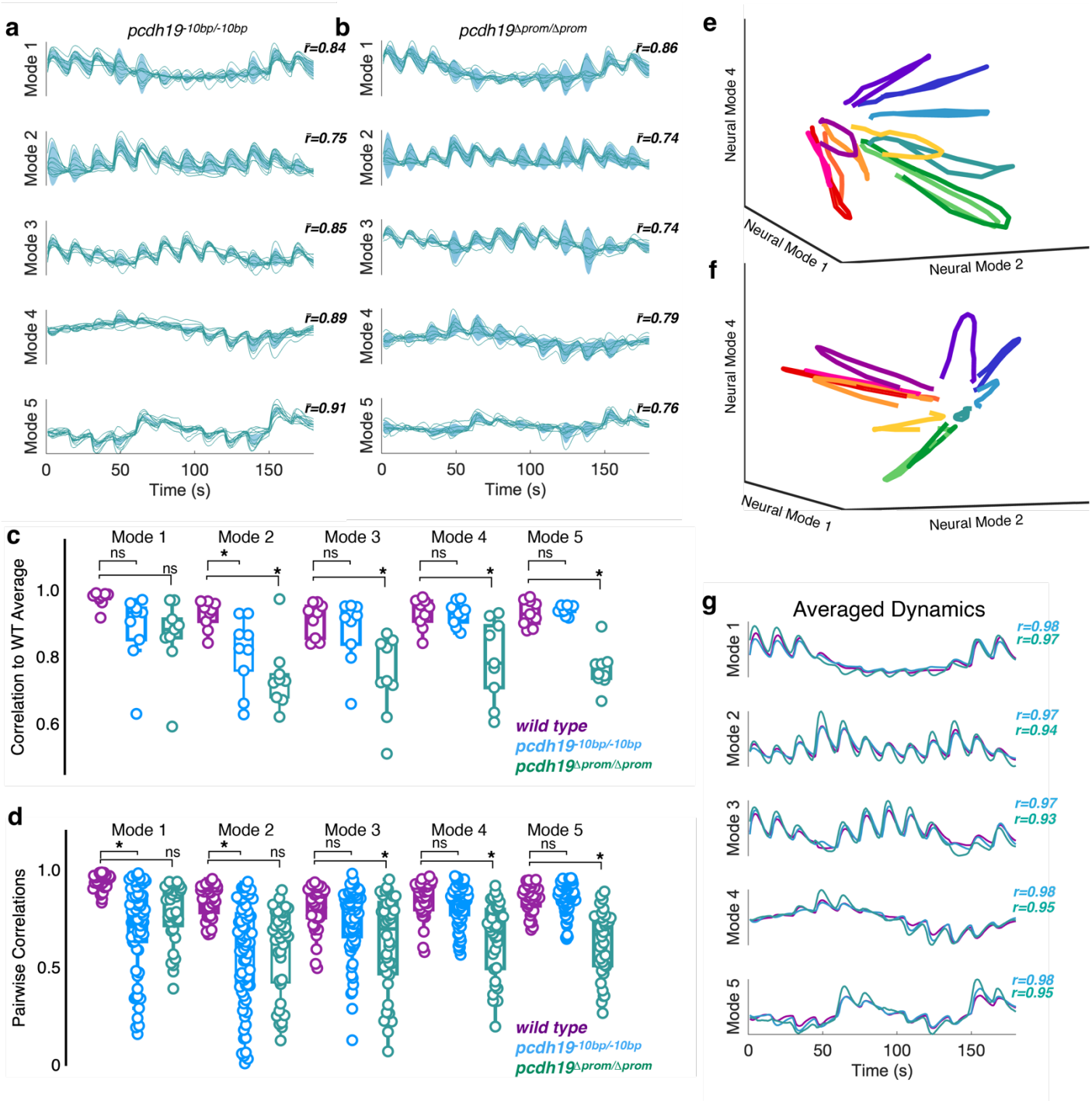

413

414
415
416
417
418
419
420
421

Figure 3. Mutations in pcdh19 lead to altered neural dynamics.

a,b. *Shown are latent dynamics determined from trial averaged neural data collected in homozygous pcdh19^{-10bp}* (***a***) and *pcdh19$^{\Delta prom}$* (***b***) *mutant larvae. Individual traces are in teal and the shaded area in blue indicates the group variance. The value, $\bar{r}$, represents the mean correlation of each individual neural mode to the group averaged neural mode.*

c. *Boxplot shows the correlation of individual trial-averaged neural modes to the wild type average (wild type, n=9: 0.97±0.008, mode 1; 0.93±0.014, mode 2; 0.91±0.017, mode 3; 0.93±0.015, mode 4; 0.93±0.013, mode 5; pcdh19^{-10bp}, n=12: 0.84±0.035, mode 1; 0.75±0.03, mode 2; 0.85±0.027, mode 3; 0.89±0.014, mode 4; 0.91±0.015, mode 5; pcdh19$^{\Delta prom}$, n=9: 0.88±0.03, mode 1; 0.78±0.04, mode 2; 0.77±0.046, mode 3; 0.80±0.04, mode 4; 0.78±0.022, mode 5; *p<0.05, Dunnett's test).*

d. *Pairwise within-group correlations of neural modes for each genotype (wild type,n=36: 0.94±0.013, mode 1; 0.84±0.028, mode 2; 0.81±0.038, mode 3; 0.85±0.031, mode 4; 0.85±0.023, mode 5; pcdh19^{-10bp}, n=66: 0.71±0.064, mode 1; 0.56±0.076, mode 2; 074±0.051, mode 3; 0.82±0.03, mode 4; 0.86±0.022, mode 5 ; pcdh19$^{\Delta prom}$, n=36: 0.78±0.05, mode 1; 0.59±0.075, mode 2; 0.61±0.095, mode 3; 0.64±0.031, mode 4; 0.63±0.056, mode 5; *p<0.05, Dunnett's test).*

e,f. *Three-dimensional representations of latent dynamics of individual pcdh19$^{\Delta prom}$ mutant larvae. The view is the same as in* ***Fig. 2g-i****.*

g. *Neural modes were averaged within each genotype (wild type/purple, pcdh19^{-10bp}/blue, pcdh19$^{\Delta prom}$/teal. The value, r, represents the correlation of each mutant average with the wild type average (pcdh19^{-10bp}/blue, pcdh19$^{\Delta prom}$/teal).*

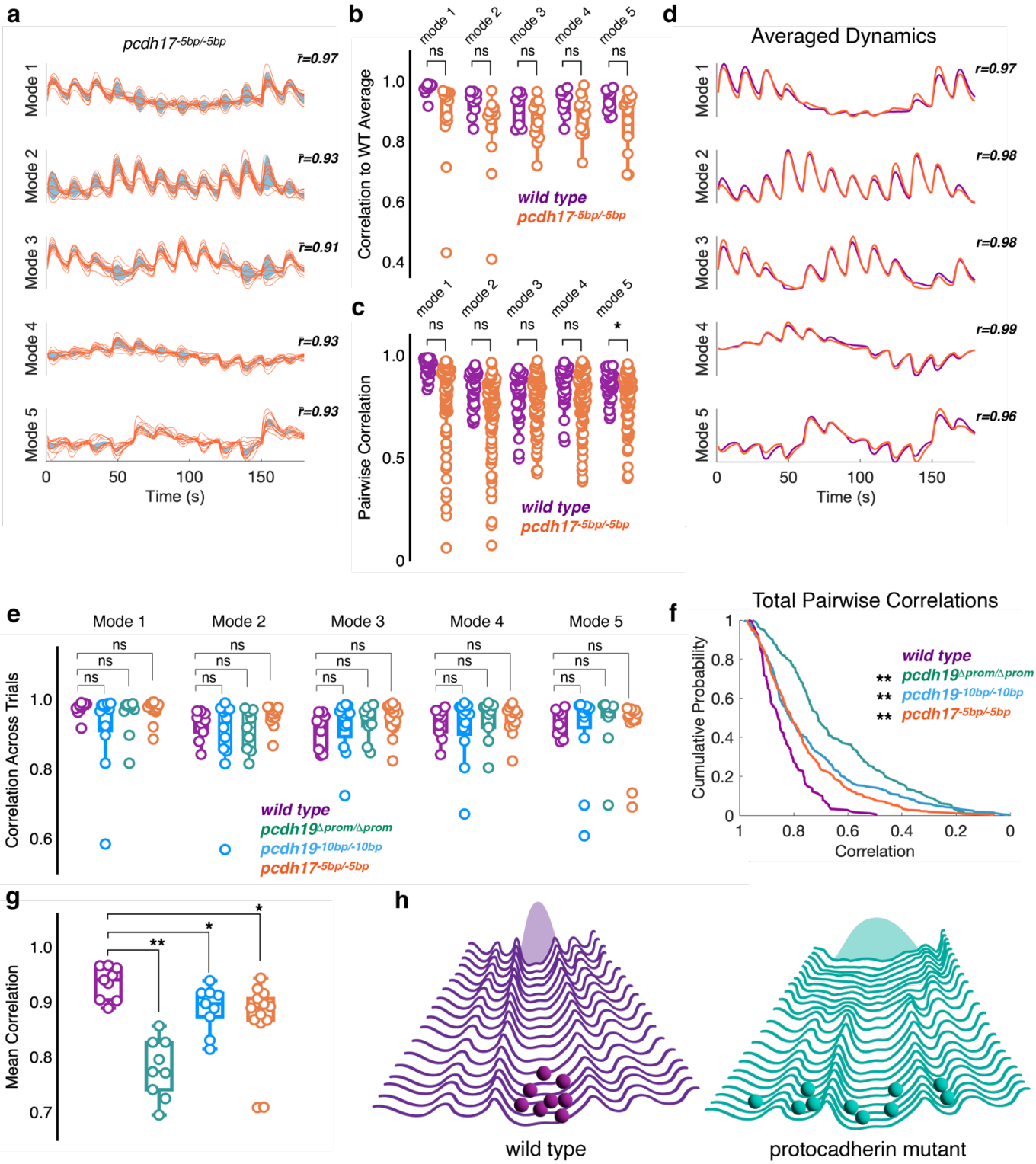
a
pcdh17-5bp/-5bp
Mode 1
Mode 2
Mode 3
Mode 4
Mode 5
r̄=0.97
r̄=0.93
r̄=0.91
r̄=0.93
r̄=0.93
0
50
100
150
Time (s)
b
mode 1
mode 2
mode 3
mode 4
mode 5
ns
Correlation to WT Average
1.0
0.8
0.6
0.4
wild type
pcdh17-5bp/-5bp
c
Pairwise Correlation
1.0
0.5
0
*
d
Averaged Dynamics
r=0.97
r=0.98
r=0.98
r=0.99
r=0.96
e
Correlation Across Trials
1.0
0.8
0.6
wild type
pcdh19Δprom/Δprom
pcdh19-10bp/-10bp
pcdh17-5bp/-5bp
f
Total Pairwise Correlations
Cumulative Probability
Correlation
**
g
Mean Correlation
1.0
0.9
0.8
0.7
h
wild type
protocadherin mutant

Figure 4. Mutations in pcdh17 lead to altered neural dynamics.

a. *Latent dynamics computed from trial averaged neural data collected in homozygous pcdh17^{-5bp} mutant larvae. Individual traces are in orange and the shaded area in blue indicates the group variance. The value, $\bar{r}$, represents the mean correlation of each individual neural mode to the group average of that neural mode.*

b. *The correlation of individual trial-averaged neural modes to the wild type average (wild type: 0.97±0.008, mode 1; 0.93±0.014, mode 2; 0.91±0.017, mode 3; 0.93±0.015, mode 4; 0.93±0.013, mode 5, n=9; pcdh17^{-5bp}: 0.87±0.042, mode 1; 0.83±0.04, mode 2; 0.87±0.019, mode 3; 0.89±0.027, mode 4; 0.87±0.093, mode 5, n=13).*

c. *Pairwise within-group correlations of neural modes for wild type (purple) and pcdh17 mutants (orange). (wild type, n=36: 0.94±0.013, mode 1; 0.84±0.028, mode 2; 0.81±0.038, mode 3; 0.85±0.031, mode 4; 0.85±0.023, mode 5; pcdh17^{-5bp}, n=78: 0.78±0.055, mode 1; 0.71±0.053, mode 2; 0.77±0.037, mode 3; 0.79±0.039, mode 4; 0.79±0.035, mode 5; *p,0.05, Dunnett's test).*

d. *Neural modes were averaged for pcdh17^{-5bp} mutants (orange) and the average was compared to the wild type average (purple). The value, $\bar{r}$, represents the correlation of each mutant average with the wild type average.*

e. *The mean trial to trial correlations are shown for wild type (purple), pcdh19^{-10bp} (blue) pcdh19$^{\Delta prom}$ (teal), and pcdh17^{-5bp} (orange) mutants. Trial-to-trial variability in the mutants is not statistically different from wild type larvae (wild type, n=9: 0.98±0.006, mode 1; 0.94±0.012, mode 2; 0.96±0.01, mode 3; 0.95±0.017, mode 4; 0.94±0.032, mode 5; pcdh19^{-10bp}: 0.92±0.034, mode 1; 0.89±0.034, mode 2; 0.92±0.022, mode 3; 0.92±0.027, mode 4; 0.91±0.036, mode 5; pcdh19$^{\Delta prom}$: 0.91±0.024, mode 1; 0.90±0.025, mode 2; 0.90±0.025, mode 3; 0.90±0.015, mode 4; 0.85±0.049, mode 5; pcdh17^{-5bp}, n=13: 0.97±0.009, mode 1; 0.95±0.009, mode 2; 0.94±0.013, mode 3; 0.94±0.012, mode 4; 0.92±0.026, mode 5).*

f. *Cumulative probability histogram for the distribution of all pairwise within group r values for wild type (purple), pcdh19^{-10bp} (blue) pcdh19$^{\Delta prom}$ (teal), and pcdh17^{-5bp} (orange) mutants. (**p<0.0001, Dunn's test).*

g. *Mean correlation (r) of individual datasets to the wild type average, averaged across neural modes (wild type, n=9: 0.90±0.018; pcdh19^{-10bp}, n=12: 0.83±0.017; pcdh19$^{\Delta prom}$, n=9: 0.74±0.033; pcdh17^{-5bp}, n=13: 0.82±0.028;*p<0.05, **p<0.0001, Dunnett's test).*

h. *Hypothesized roles of Pcdh19 and Pcdh17 in canalyzing the assembly of visual circuits in the zebrafish optic tectum. In the wild type scenario (left/purple), development is canalized and the outcomes (circuit response to visual stimulation) is restricted, showing a small distribution in outcomes (shaded Gaussian). In the case of protocadherin mutants (right/teal), the developmental landscape is flattened, allowing development to stochastically explore a variety of alternative paths, leading to an increased variation among outcomes (broad shaded distribution).*

527 **REFERENCES**
528

529 1. Waddington, C. (1942). Canalization of development and the inheritance of acquired characters. Nature
530 *150*, 563–565. https://doi.org/10.1007/s00128-015-1540-6.

531 2. Xu, T., Nenning, K.-H., Schwartz, E., Hong, S.-J., Vogelstein, J.T., Goulas, A., Fair, D.A., Schroeder,
532 C.E., Margulies, D.S., Smallwood, J., et al. (2020). Cross-species functional alignment reveals
533 evolutionary hierarchy within the connectome. NeuroImage *223*, 117346.
534 https://doi.org/10.1016/j.neuroimage.2020.117346.

535 3. Mars, R.B., Sotiropoulos, S.N., Passingham, R.E., Sallet, J., Verhagen, L., Khrapitchev, A.A., Sibson,
536 N., and Jbabdi, S. (2018). Whole brain comparative anatomy using connectivity blueprints. eLife *7*,
537 e35237. https://doi.org/10.7554/elife.35237.

538 4. Kitano, H. (2004). Biological robustness. Nature reviews Genetics *5*, 826–837.
539 https://doi.org/10.1038/nrg1471.

540 5. Masel, J., and Siegal, M.L. (2009). Robustness: mechanisms and consequences. Trends Genet. *25*, 395–
541 403. https://doi.org/10.1016/j.tig.2009.07.005.

542 6. Geschwind, D.H., and Levitt, P. (2007). Autism spectrum disorders: developmental disconnection
543 syndromes. Current opinion in neurobiology *17*, 103–111. https://doi.org/10.1016/j.conb.2007.01.009.

544 7. Yamasaki, T., Maekawa, T., Fujita, T., and Tobimatsu, S. (2017). Connectopathy in Autism Spectrum
545 Disorders: A Review of Evidence from Visual Evoked Potentials and Diffusion Magnetic Resonance
546 Imaging. Frontiers in neuroscience *11*, 158–14. https://doi.org/10.3389/fnins.2017.00627.

547 8. Lynall, M.-E., Bassett, D.S., Kerwin, R., McKenna, P.J., Kitzbichler, M., Müller, U., and Bullmore, E.
548 (2010). Functional connectivity and brain networks in schizophrenia. Journal of Neuroscience *30*, 9477–
549 9487. https://doi.org/10.1523/jneurosci.0333-10.2010.

550 9. Friston, K., Brown, H.R., Siemerkus, J., and Stephan, K.E. (2016). The dysconnection hypothesis
551 (2016). Schizophrenia Research *176*, 83–94. https://doi.org/10.1016/j.schres.2016.07.014.

552 10. Belmonte, M.K., Allen, G., Beckel-Mitchener, A., Boulanger, L.M., Carper, R.A., and Webb, S.J.
553 (2004). Autism and abnormal development of brain connectivity. Journal of Neuroscience *24*, 9228–9231.
554 https://doi.org/10.1523/jneurosci.3340-04.2004.

555 11. Woodbury-Smith, M., Nicolson, R., Zarrei, M., Yuen, R.K.C., Walker, S., Howe, J., Uddin, M.,
556 Hoang, N., Buchanan, J.A., Chrysler, C., et al. (2017). Variable phenotype expression in a family
557 segregating microdeletions of the NRXN1 and MBD5 autism spectrum disorder susceptibility genes. npj
558 Genom. Med. *2*, 17. https://doi.org/10.1038/s41525-017-0020-9.

559 12. Masfrand, S. de, Cogné, B., Nizon, M., Deb, W., Goldenberg, A., Lecoquierre, F., Nicolas, G.,
560 Bournez, M., Vitobello, A., Mau-Them, F.T., et al. (2024). Penetrance, variable expressivity and
561 monogenic neurodevelopmental disorders. Eur. J. Méd. Genet. *69*, 104932.
562 https://doi.org/10.1016/j.ejmg.2024.104932.

563 13. Chien, Y., Wu, C., and Tsai, H. (2021). The Comorbidity of Schizophrenia Spectrum and Mood
564 Disorders in Autism Spectrum Disorder. Autism Res. *14*, 571–581. https://doi.org/10.1002/aur.2451.

565 14. Cristino, A.S., Williams, S.M., Hawi, Z., An, J.-Y., Bellgrove, M.A., Schwartz, C.E., Costa, L. da F.,
566 and Claudianos, C. (2013). Neurodevelopmental and neuropsychiatric disorders represent an
567 interconnected molecular system. Molecular psychiatry *19*, 294–301. https://doi.org/10.1038/mp.2013.16.

568 15. Hamlyn, J., Duhig, M., McGrath, J., and Scott, J. (2013). Modifiable risk factors for schizophrenia
569 and autism - Shared risk factors impacting on brain development. Neurobiology of disease *53*, 3–9.
570 https://doi.org/10.1016/j.nbd.2012.10.023.

571 16. Zhu, X., Need, A.C., Petrovski, S., and Goldstein, D.B. (2014). One gene, many neuropsychiatric
572 disorders: lessons from Mendelian diseases. Nature Publishing Group *17*, 773–781.
573 https://doi.org/10.1038/nn.3713.

574 17. Hulpiau, P., and Roy, F.V. (2009). Molecular evolution of the cadherin superfamily. The international
575 journal of biochemistry & cell biology *41*, 349–369. https://doi.org/10.1016/j.biocel.2008.09.027.

576 18. Nollet, F., Kools, P., and Roy, F. van (2000). Phylogenetic analysis of the cadherin superfamily
577 allows identification of six major subfamilies besides several solitary members. Journal of Molecular
578 Biology *299*, 551–572. https://doi.org/10.1006/jmbi.2000.3777.

579 19. Jontes, J.D. (2017). The Cadherin Superfamily in Neural Circuit Assembly. Cold Spring Harbor
580 perspectives in biology *10*, a029306. https://doi.org/10.1101/cshperspect.a029306.

581 20. Piton, A., Gauthier, J., Hamdan, F.F., Lafrenière, R.G., Yang, Y., Henrion, E., Laurent, S., Noreau,
582 A., Thibodeau, P., Karemera, L., et al. (2011). Systematic resequencing of X-chromosome synaptic genes
583 in autism spectrum disorder and schizophrenia. Molecular psychiatry *16*, 867–880.
584 https://doi.org/10.1038/mp.2010.54.

585 21. Vlaskamp, D.R.M., Bassett, A.S., Sullivan, J.E., Robblee, J., Sadleir, L.G., Scheffer, I.E., and
586 Andrade, D.M. (2019). Schizophrenia is a later-onset feature of PCDH19Girls Clustering Epilepsy.
587 Epilepsia *60*, 429–440. https://doi.org/10.1111/epi.14678.

588 22. Dibbens, L.M., Tarpey, P.S., Hynes, K., Bayly, M.A., Scheffer, I.E., Smith, R., Bomar, J., Sutton, E.,
589 Vandeleur, L., Shoubridge, C., et al. (2008). X-linked protocadherin 19 mutations cause female-limited
590 epilepsy and cognitive impairment. Nature Genetics *40*, 776–781. https://doi.org/10.1038/ng.149.

591 23. Depienne, C., Depienne, C., Bouteiller, D., Bouteiller, D., Keren, B., Keren, B., Cheuret, E., Cheuret,
592 E., Poirier, K., Poirier, K., et al. (2009). Sporadic Infantile Epileptic Encephalopathy Caused by
593 Mutations in PCDH19 Resembles Dravet Syndrome but Mainly Affects Females. PLoS Genetics *5*,
594 e1000381. https://doi.org/10.1371/journal.pgen.1000381.t001.

595 24. Bollmann, J.H., and Engert, F. (2009). Subcellular Topography of Visually Driven Dendritic Activity
596 in the Vertebrate Visual System. Neuron *61*, 895–905. https://doi.org/10.1016/j.neuron.2009.01.018.

597 25. Niell, C.M., and Smith, S.J. (2005). Functional imaging reveals rapid development of visual response
598 properties in the zebrafish tectum. Neuron *45*, 941–951. https://doi.org/10.1016/j.neuron.2005.01.047.

26. Baier, H., and Scott, E.K. (2024). The Visual Systems of Zebrafish. Annu. Rev. Neurosci. *47*, 255–276. https://doi.org/10.1146/annurev-neuro-111020-104854.

27. Förster, D., Helmbrecht, T.O., Mearns, D.S., Jordan, L., Mokayes, N., and Baier, H. (2020). Retinotectal circuitry of larval zebrafish is adapted to detection and pursuit of prey. Elife *9*, e58596. https://doi.org/10.7554/elife.58596.

28. Giovannucci, A., Friedrich, J., Gunn, P., Kalfon, J., Brown, B.L., Koay, S.A., Taxidis, J., Najafi, F., Gauthier, J.L., Zhou, P., et al. (2019). CaImAn an open source tool for scalable calcium imaging data analysis. eLife *8*, e38173. https://doi.org/10.7554/elife.38173.

29. Vyas, S., Golub, M.D., Sussillo, D., and Shenoy, K.V. (2020). Computation Through Neural Population Dynamics. Annu Rev Neurosci *43*, 249–275. https://doi.org/10.1146/annurev-neuro-092619-094115.

30. Saxena, S., and Cunningham, J.P. (2019). Towards the neural population doctrine. Curr. Opin. Neurobiol. *55*, 103–111. https://doi.org/10.1016/j.conb.2019.02.002.

31. Langdon, C., Genkin, M., and Engel, T.A. (2023). A unifying perspective on neural manifolds and circuits for cognition. Nat. Rev. Neurosci. *24*, 363–377. https://doi.org/10.1038/s41583-023-00693-x.

32. Sadtler, P.T., Quick, K.M., Golub, M.D., Chase, S.M., Ryu, S.I., Tyler-Kabara, E.C., Yu, B.M., and Batista, A.P. (2014). Neural constraints on learning. Nature *512*, 423–426. https://doi.org/10.1038/nature13665.

33. Gallego, J.A., Perich, M.G., Miller, L.E., and Solla, S.A. (2017). Neural Manifolds for the Control of Movement. Neuron *94*, 978–984. https://doi.org/10.1016/j.neuron.2017.05.025.

34. Safaie, M., Chang, J.C., Park, J., Miller, L.E., Dudman, J.T., Perich, M.G., and Gallego, J.A. (2023). Preserved neural dynamics across animals performing similar behaviour. Nature *623*, 765–771. https://doi.org/10.1038/s41586-023-06714-0.

35. Gallego, J.A., Perich, M.G., Chowdhury, R.H., Solla, S.A., and Miller, L.E. (2020). Long-term stability of cortical population dynamics underlying consistent behavior. Nat. Neurosci. *23*, 260–270. https://doi.org/10.1038/s41593-019-0555-4.

36. Cooper, S.R., Emond, M.R., Duy, P.Q., Liebau, B.G., Wolman, M.A., and Jontes, J.D. (2015). Protocadherins control the modular assembly of neuronal columns in the zebrafish optic tectum. J Cell Biol *211*, 807–814. https://doi.org/10.1083/jcb.201507108.

37. Biswas, S., Emond, M.R., Chenoweth, K.P., and Jontes, J.D. (2021). δ-Protocadherins regulate neural progenitor cell division by antagonizing Ryk and Wnt/β-catenin signaling. Iscience *24*, 102932. https://doi.org/10.1016/j.isci.2021.102932.

38. El-Brolosy, M.A., Kontarakis, Z., Rossi, A., Kuenne, C., Günther, S., Fukuda, N., Kikhi, K., Boezio, G.L.M., Takacs, C.M., Lai, S.-L., et al. (2019). Genetic compensation triggered by mutant mRNA degradation. Nature *568*, 193–197. https://doi.org/10.1038/s41586-019-1064-z.

634 39. Rossi, A., Kontarakis, Z., Gerri, C., Nolte, H., Hölper, S., Krüger, M., and Stainier, D.Y.R. (2015).
635 Genetic compensation induced by deleterious mutations but not gene knockdowns. Nature *524*, 230–233.
636 https://doi.org/10.1038/nature14580.

637 40. Redies, C., Hertel, N., and Hübner, C.A. (2012). Cadherins and neuropsychiatric disorders. Brain
638 research *1470*, 130–144. https://doi.org/10.1016/j.brainres.2012.06.020.

639 41. Hirano, S., and Takeichi, M. (2012). Cadherins in Brain Morphogenesis and Wiring. Physiological
640 reviews *92*, 597–634. https://doi.org/10.1152/physrev.00014.2011.

641 42. Tsai, N.-P., Wilkerson, J.R., Guo, W., Maksimova, M.A., Demartino, G.N., Cowan, C.W., and Huber,
642 K.M. (2012). Multiple Autism-Linked Genes Mediate Synapse Elimination via Proteasomal Degradation
643 of a Synaptic Scaffold PSD-95. Cell *151*, 1581–1594. https://doi.org/10.1016/j.cell.2012.11.040.

644 43. Morrow, E.M., Morrow, E.M., Yoo, S.-Y., Yoo, S.-Y., Flavell, S.W., Flavell, S.W., Kim, T.-K., Kim,
645 T.-K., Lin, Y., Lin, Y., et al. (2008). Identifying autism loci and genes by tracing recent shared ancestry.
646 Science (New York, NY) *321*, 218–223. https://doi.org/10.1126/science.1157657.

647 44. Kasnauskiene, J., Kasnauskiene, J., Ciuladaite, Z., Ciuladaite, Z., Preiksaitiene, E., Preiksaitiene, E.,
648 Matulevičienė, A., Matulevičienė, A., Alexandrou, A., Alexandrou, A., et al. (2012). A single gene
649 deletion on 4q28.3: PCDH18 - A new candidate gene for intellectual disability? European Journal of
650 Medical Genetics *55*, 1–4. https://doi.org/10.1016/j.ejmg.2012.02.010.

651 45. Chang, H., Hoshina, N., Zhang, C., Ma, Y., Cao, H., Wang, Y., Wu, D., Bergen, S.E., n, M.L. eacute,
652 Hultman, C.M., et al. (2017). The protocadherin 17 gene affects cognition, personality, amygdala
653 structure and function, synapse development and risk of major mood disorders. Molecular psychiatry *23*,
654 1–13. https://doi.org/10.1038/mp.2016.231.

655 46. Light, S.E.W., and Jontes, J.D. (2019). Multiplane calcium imaging reveals disrupted development of
656 network topology in zebrafish pcdh19 mutants. Eneuro *6*, ENEURO.0420-18.2019.
657 https://doi.org/10.1523/eneuro.0420-18.2019.

658 47. Giansante, G., Mazzoleni, S., Zippo, A.G., Ponzoni, L., Ghilardi, A., Maiellano, G., Lewerissa, E.,
659 Hugte, E. van, Kasri, N.N., Francolini, M., et al. (2023). Neuronal network activity and connectivity are
660 impaired in a conditional knockout mouse model with PCDH19 mosaic expression. Mol Psychiatr, 1–16.
661 https://doi.org/10.1038/s41380-023-02022-1.

662 48. Robens, B.K., Yang, X., McGraw, C.M., Turner, L.H., Robens, C., Thyme, S., Rotenberg, A., and
663 Poduri, A. (2022). Mosaic and non-mosaic protocadherin 19 mutation leads to neuronal hyperexcitability
664 in zebrafish. Neurobiol Dis *169*, 105738–105738. https://doi.org/10.1016/j.nbd.2022.105738.

665 49. Hallgrimsson, B., Green, R.M., Katz, D.C., Fish, J.L., Bernier, F.P., Roseman, C.C., Young, N.M.,
666 Cheverud, J.M., and Marcucio, R.S. (2019). The developmental-genetics of canalization. Semin. Cell
667 Dev. Biol. *88*, 67–79. https://doi.org/10.1016/j.semcdb.2018.05.019.

668 50. Siegal, M.L., and Bergman, A. (2002). Waddington's canalization revisited: developmental stability
669 and evolution. Proceedings of the National Academy of Sciences of the United States of America *99*,
670 10528–10532. https://doi.org/10.1073/pnas.102303999.

51. Pologruto, T.A., Sabatini, B.L., and Svoboda, K. (2003). ScanImage: flexible software for operating laser scanning microscopes. Biomedical engineering online *2*, 13. https://doi.org/10.1186/1475-925x-2-13.

52. Romano, S.A., Pietri, T., Pérez-Schuster, V., Jouary, A., Haudrechy, M., and Sumbre, G. (2015). Spontaneous Neuronal Network Dynamics Reveal Circuit's Functional Adaptations for Behavior. Neuron *85*, 1070–1085. https://doi.org/10.1016/j.neuron.2015.01.027.

53. Avitan, L., Pujic, Z., Mölter, J., Poll, M.V.D., Sun, B., Teng, H., Amor, R., Scott, E.K., and Goodhill, G.J. (2017). Spontaneous Activity in the Zebrafish Tectum Reorganizes over Development and Is Influenced by Visual Experience. Current Biology *27*, 2407-2419.e4. https://doi.org/10.1016/j.cub.2017.06.056.

54. Gabriel, J.P., Trivedi, C.A., Maurer, C.M., Ryu, S., and Bollmann, J.H. (2012). Layer-specific targeting of direction-selective neurons in the zebrafish optic tectum. Neuron *76*, 1147–1160. https://doi.org/10.1016/j.neuron.2012.12.003.

55. Pnevmatikakis, E.A., and Giovannucci, A. (2017). NoRMCorre: An online algorithm for piecewise rigid motion correction of calcium imaging data. Journal of neuroscience methods *291*, 83–94. https://doi.org/10.1016/j.jneumeth.2017.07.031.